(Received 20 March 2026, Accepted 24 April 2026, Scheduled 11 May 2026)

A Flexible Hybrid Rectenna with Frequency-Domain Complementarity for RF Energy Harvesting and WPT

Lei Li[1,2,*], Yang Hu[1,2], Yuting Jia[1,2], Xiaomeng Wang[1,2], Yanting Wang[1,2], Enxin Zhao[1,2], Shulin Li[1,2], and Jingchang Nan[1,2]

[1]*School of Electronics and Information Engineering, Liaoning Technical University, Huludao 125105, China*
[2]*Liaoning Key Laboratory of Radio Frequency and Big Data for Intelligent Applications, Huludao 125105, China*

ABSTRACT: A novel flexible hybrid rectenna for simultaneous RF energy harvesting (RF-EH) and dedicated wireless power transfer (WPT) is proposed in this study. The rectenna comprises a notched broadband omnidirectional microstrip antenna (2.8–6.3 GHz with a 4.7 GHz notch) and a 4.7 GHz directional dielectric resonator antenna (DRA) located on the microstrip antenna. At the 4.7 GHz notch band, electromagnetic energy is confined around an L-shaped strip and a split-ring slot of the microstrip antenna, exciting the TM^{z}_{201} resonant mode in the DRA, which produces a narrow radiation beam at 4.7 GHz. This enables a frequency-domain complementary operation: ambient energy is harvested across the broadband region for low-power applications, whereas dedicated power is efficiently received at 4.7 GHz for high-power operation. A broadband rectifier employing a dual-channel impedance matching architecture is proposed, in which two parallel branches cooperatively extend the rectification bandwidth. Measurements demonstrate that the rectenna achieves efficiencies above 45% across 2.8–6.3 GHz, with a peak efficiency of 57.9%. In addition, the use of polydimethylsiloxane (PDMS) as the substrate provides high flexibility and excellent conformability, making the proposed rectenna well-suited for powering electronics on curved surfaces, compact devices, and curved-surface Internet-of-Things (IoT) nodes, such as robots, drones, in-vehicle applications, and industrial robotic arm units, enabling reliable conformal deployment on non-planar equipment and distributed IoT systems.

1. INTRODUCTION

The rapid growth of the Internet of Things (IoT) has driven the massive proliferation of interconnected electronic devices and sensors [1]. In the future, billions of wireless sensors are expected to operate in a self-powered and batteryless manner, making radio frequency energy harvesting (RF-EH) and wireless power transfer (WPT) promising solutions [2]. Many of these sensors are deployed on curved or non-planar surfaces (e.g., robots, drones, in-vehicle applications, and industrial robotic arm units), requiring conformal antenna integration to preserve mechanical flexibility and system performance.

The performance requirements for receiving antennas vary significantly between RF-EH and WPT systems. Ambient RF energy is widely distributed across major communication bands, such as the 2G/3G/4G/5G and ISM bands. However, they are characterized by low power density and unpredictable incident directions. Accordingly, antennas for RF-EH systems have been extensively studied to improve energy capture through various approaches, such as bandwidth expansion [3–8], polarization diversity [9, 10], and enhanced spatial coverage [11–14]. In contrast, WPT operates with a dedicated source at a specific frequency and direction, requiring antennas with high gain [15, 16] and strong directivity [17–19] to efficiently focus the energy on the receiving devices.

The integration of RF-EH with WPT enables simultaneous wide area ambient energy harvesting and efficient directional power transfer, providing a continuous, stable, and adaptive hybrid power solution for IoT devices and wireless sensor nodes. From the perspective of a receiving antenna design, the integration of RF-EH and WPT has been investigated in [20–22]. In both [20] and [21], receiving antennas utilize a broadband omnidirectional mode for RF-EH (2.03–4.08 GHz and 1.55–3.66 GHz, respectively), along with an independent high-directivity mode at 5.8 GHz for directional WPT. In [20], RF-EH and WPT modes are simultaneously achieved by loading patches and shorting vias on a back-to-back microstrip antenna, whereas [21] realizes dual radiation modes by combining two orthogonal antennas. However, the RF-EH receiving antenna typically operates over a limited frequency band. Excessive bandwidth expansion will overlap with the WPT operating band, leading to radiation pattern interference. In [22], a multiband dual-polarized hybrid antenna is suggested as a solution to this problem. Spatially complementary beams are produced by placing the directional beam within the null of the omnidirectional pattern, enabling RF-EH and WPT to coexist within the shared 2.45 GHz band. However, the beam-nested design is challenged by structural complexity and inherent interference between omnidirectional and directional beams. To address this challenge, this paper proposes a frequency-domain complementary approach that employs a notched broadband omnidirectional microstrip antenna for RF-EH and a directional di-

* Corresponding author: Lei Li (lntuicgroup@163.com).

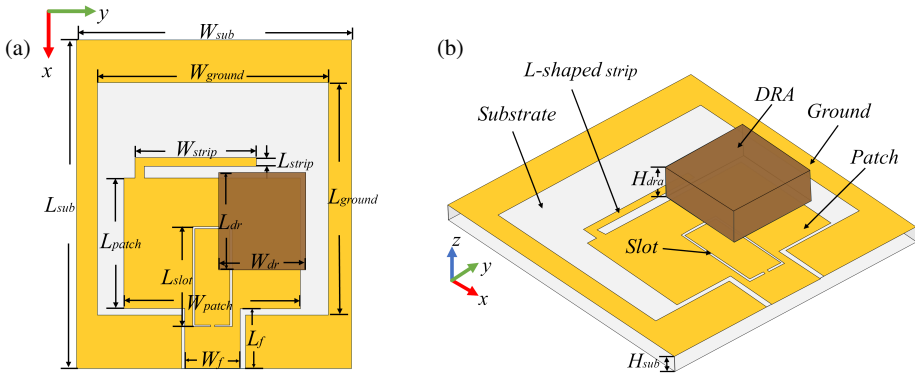

FIGURE 1. The geometric structure of the antenna. (a) Top view, (b) 3D view.

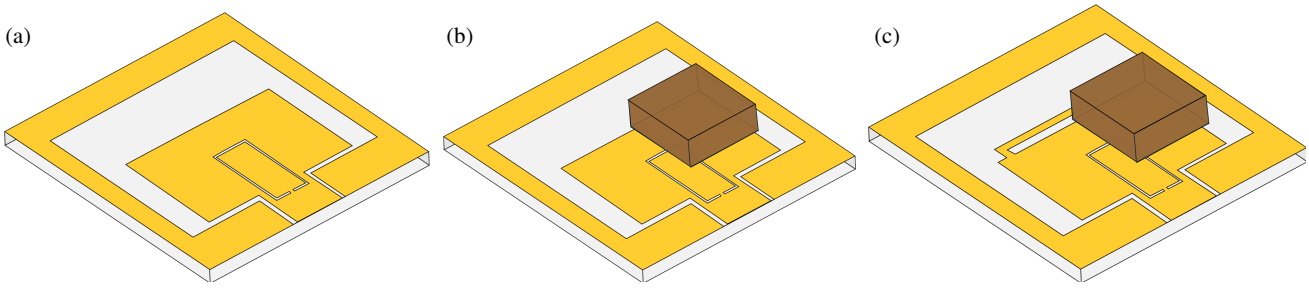

FIGURE 2. The design process of the antenna. (a) Antenna 1, (b) Antenna 2, (c) Antenna 3.

TABLE 1. Dimensions of the designed antenna (unit: mm).

Parameters	Value	Parameters	Value	Parameters	Value
W_{sub}	30	L_{sub}	25	W_{strip}	11
W_{ground}	21	L_{ground}	21	L_{strip}	0.8
W_{patch}	16	L_{patch}	12	H_{sub}	0.6
W_f	5	L_f	4.7	L_{slot}	9.2
W_{dr}	8	L_{dr}	9	H_{dra}	3

electric resonator antenna (DRA) excited at the notch band for WPT.

Furthermore, although traditional rigid antennas offer excellent electrical performance, they fail to satisfy the flexibility requirements of complex geometries and distributed IoT nodes. Polydimethylsiloxane (PDMS) is an attractive substrate for conformal and lightweight antennas [23–26]. Accordingly, the proposed RF-EH/WPT system was implemented on a PDMS substrate, enabling enhanced adaptability and deployability on complex and irregular surfaces, with promising potential in emerging applications, such as smart IoT, robotics, and aerospace.

In this study, a coplanar waveguide (CPW)-fed microstrip antenna incorporating an L-shaped strip and a split-ring slot is designed to achieve an omnidirectional radiation pattern and a notched broadband response (2.8–6.3 GHz with a 4.7 GHz notch). The DRA is positioned above the L-shaped strip and split-ring slot. The concentrated near-field distribution at 4.7 GHz excited the TM^{z}_{201} resonant mode in the DRA, producing a narrow directional radiation pattern. This frequency-domain complementary operation enables wideband ambient RF-EH using the microstrip antenna while supporting dedicated, efficient WPT at 4.7 GHz via the DRA. The gains of the broadband microstrip antenna at 3.6 GHz, 4.0 GHz, and 5.8 GHz are 3.18 dBi, 3.02 dBi, and 6.12 dBi, respectively, and the antenna exhibits a gain of 4.28 dBi at the 4.7 GHz notch frequency. A broadband rectifier based on dual-channel impedance matching is proposed, employing two parallel branches to extend the rectification bandwidth. The efficiency of the rectenna in the 2.8–6.3 GHz frequency band exceeded 45%, with a peak efficiency of 57.9%. In addition, the rectenna was fabricated on a PDMS substrate, which provides high flexibility and excellent conformability.

2. ANTENNA DESIGN

2.1. The Structure of Antenna

The overall shape of the proposed antenna element, which uses a "microstrip-DR" composite antenna structure, is shown in Fig. 1. The antenna was fabricated on a flexible PDMS substrate that measures $30 \times 25 \times 0.6\,\text{mm}^3$ ($\varepsilon_r = 2.7$, $\tan\delta = 0.03$). The radiating patch has a rectangular monopole configuration fed via a CPW. The rectangular DRA ($\varepsilon_r = 12.3$, $\tan\delta = 0.00014$) had dimensions of $9 \times 8 \times 3\,\text{mm}^3$. The optimized key structural parameters are listed in Table 1.

2.2. Design Process of the Antenna

Figure 2 shows the antenna's evolutionary design, while Fig. 3 plots the accompanying S_{11}, gain, and radiation efficiency results. Initially, a CPW-fed rectangular patch performs as a

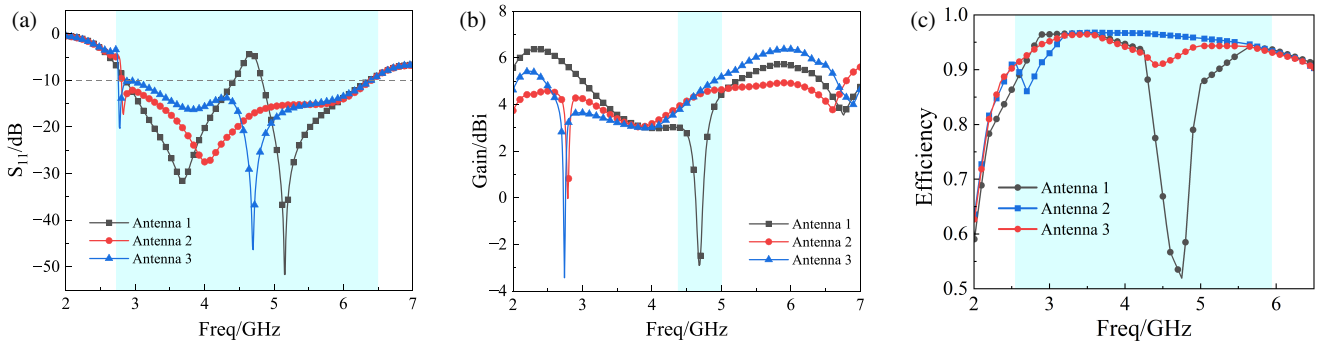

FIGURE 3. S_{11} and gain of the three antennas shown in Fig. 2. (a) S_{11} of three antennas. (b) Gain of three antennas. (c) Radiation efficiency of three antennas.

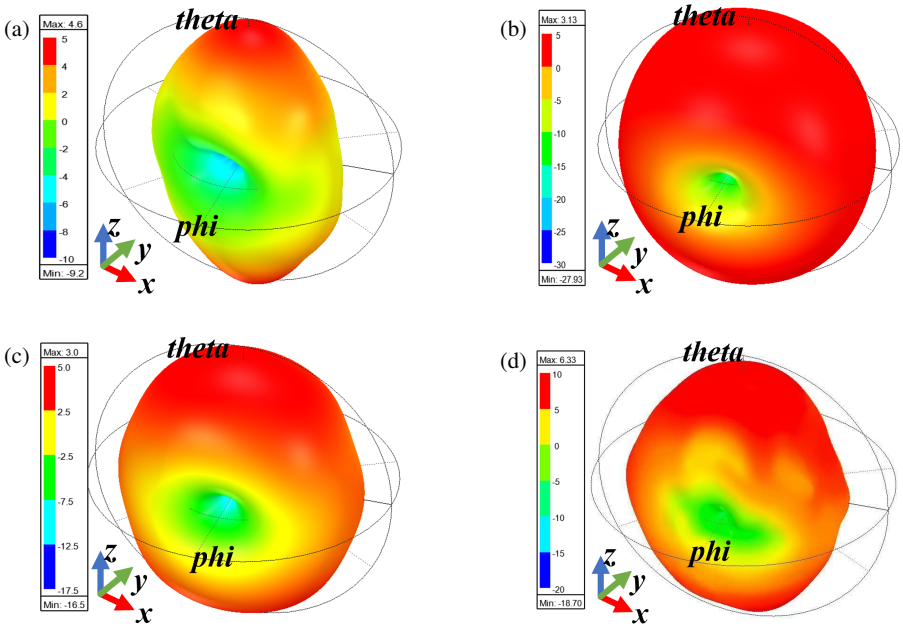

FIGURE 4. 3D radiation patterns at (a) 4.7 GHz, (b) 3.6 GHz, (c) 4 GHz, (d) 5.8 GHz.

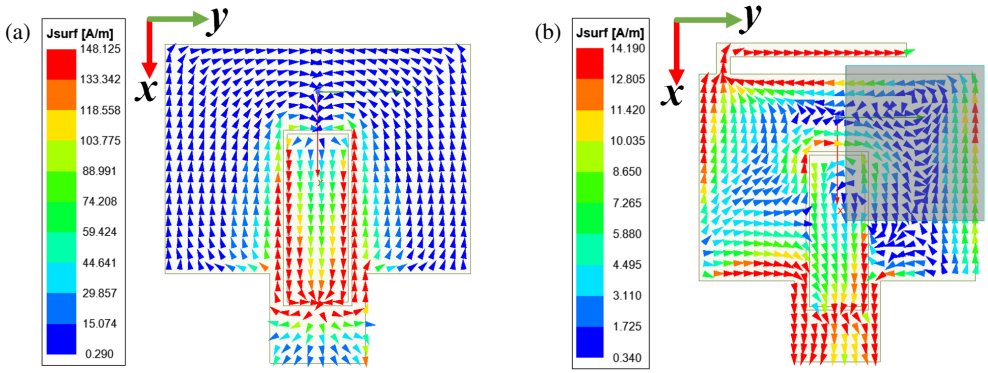

FIGURE 5. Current distribution of (a) Antenna 1, (b) Antenna 3.

broadband monopole antenna. Introducing the slot produces a notched broadband antenna with a notch at 4.7 GHz. To obtain directional radiation at 4.7 GHz, a DRA is placed directly above the slot, forming the antenna shown in Fig. 2(b). The S_{11} and gain in Fig. 3 confirm that the DRA is slot-fed and resonates at 4.7 GHz, but its directivity is insufficient to meet the strong directional requirements for WPT.

To address this, an L-shaped strip is introduced at the top of the notch antenna, forming Antenna 3 shown in Fig. 2(c). At 4.7 GHz, coupling via the slot and the gap between the L-shaped strip and the radiating edge excites the DRA, yield-

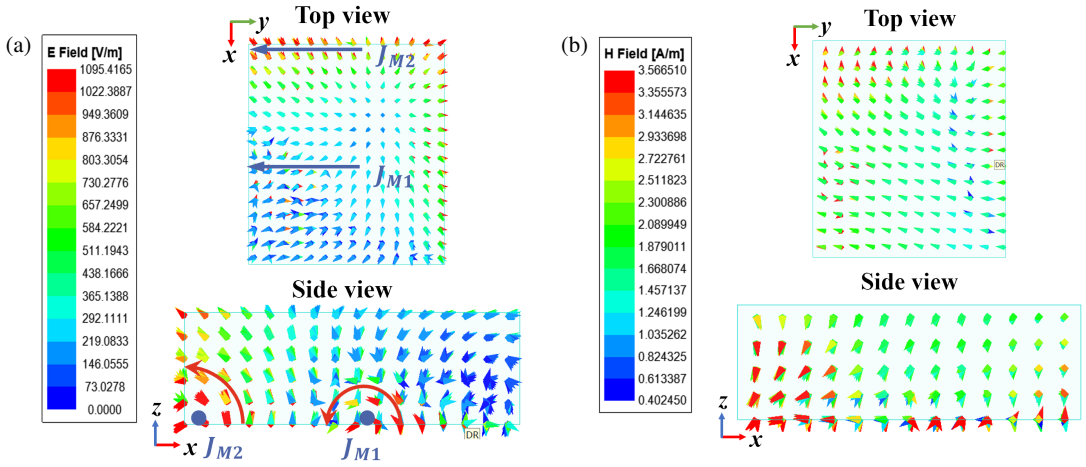

FIGURE 6. Electric and magnetic field distributions of DRA in Antenna 3. (a) E-field, (b) H-field.

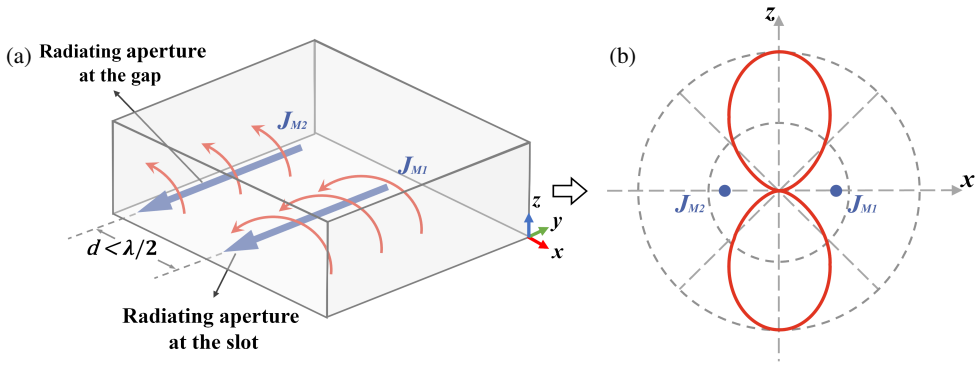

FIGURE 7. Working principle of magnetic dipole array antenna.

ing a more directional radiation pattern and increasing the gain from −2.7 dBi (notch-band) to 4.6 dBi, and improving the corresponding radiation efficiency of the antenna from 53.5% to 92.6%. This enables Antenna 3 to perform directional WPT at 4.7 GHz while maintaining near-omnidirectional RF-EH across the remaining frequency bands, successfully integrating both functions. The results are shown in Fig. 4.

2.3. Theoretical Analysis

Antenna 1 in Fig. 2(a) was formed, achieving a frequency band suppression of 4.7 GHz in the broadband range. The notch characteristic is realized by etching a rectangular split-ring slot in the radiation patch of the monopole antenna. The length of the slot is usually $\lambda/4$, determined by the following formula [27]:

$$L = \frac{C}{4f_c \cdot \sqrt{\varepsilon_{eff}}} \tag{1}$$

where C is the velocity of light, f_c the center frequency of the notch band, and ε_{eff} the effective dielectric constant of the composite.

This slot structure excites a half-wavelength resonance at 4.7 GHz. As shown in Fig. 5(a), the current generated by this resonance is out of phase with the main patch current, resulting in mutual cancellation and effective radiation suppression at this frequency.

As shown in Fig. 5(b), opposite surface currents are distributed around the slot and the gap between the L-shaped strip and the radiating edge, which induces a strong localized electric field across the slot and the gap. The intense near-field energy acts as a 'feed source', driving the DRA to operate in the TM^z_{201} mode. Fig. 6 shows the electric and magnetic field distributions within the DRA. The DRA comprises two electric field vortices and a corresponding magnetic field, which can be

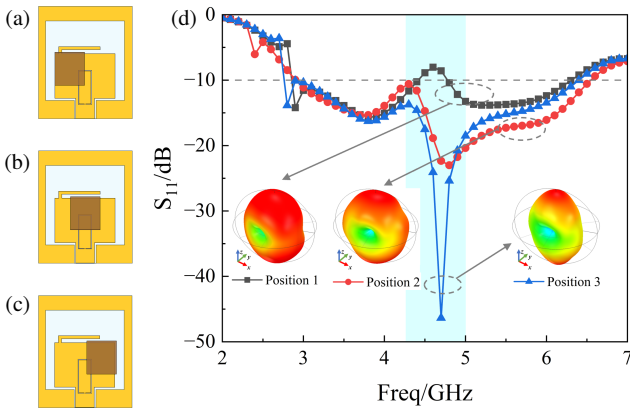

FIGURE 8. Effect of different positions of DR on the antenna. (a) Position 1, (b) Position 2, (c) Position 3, (d) S_{11} and 3D radiation pattern of antennas.

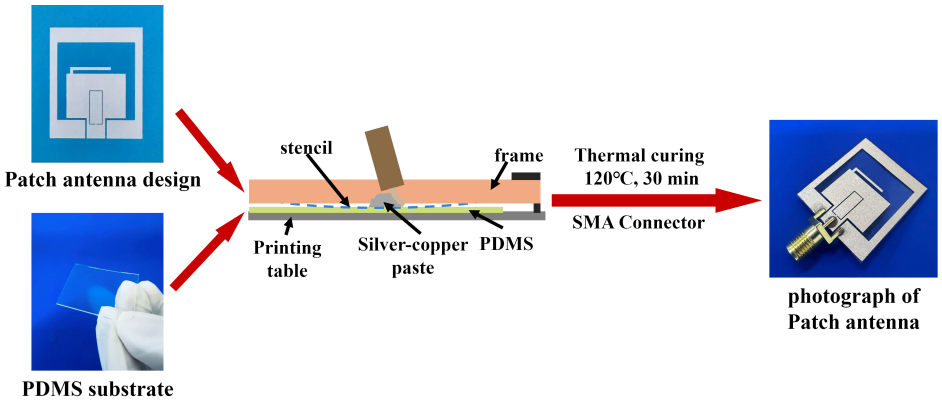

FIGURE 9. Schematic diagram of the manufacturing process of the patch antenna.

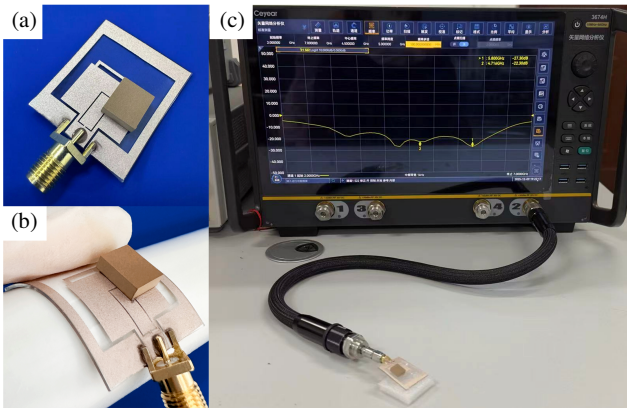

FIGURE 10. The details of the fabricated antenna. (a) Antenna on a plane surface. (b) Antenna on a curved surface. (c) Experimental setup for measured S_{11}.

equivalently modeled as two parallel magnetic dipoles (J_{M1} and J_{M2}). With a spacing less than half a wavelength, these dipoles form a two-element array structure. This ultimately generates directional narrow-beam radiation, leading to an enhanced directivity at 4.7 GHz. A schematic of the working principle is shown in Fig. 7.

To examine the influence of key structural parameters, the effect of varying the placement of the DRA was analyzed. Fig. 8 reveals that different positions of the DRA produce distinct S_{11} values and directional patterns at 4.7 GHz, with optimal directivity achievable only when the DRA is positioned at Position 3.

2.4. Construction and Testing of the Antenna

A microstrip antenna was created and manufactured on a PDMS substrate with a liquid silver-copper paste. The procedure is shown in Fig. 9. First, based on the designed model, the antenna pattern was printed onto the PDMS using silkscreen. The printed antenna pattern was then thermally cured at 120°C for 30 minutes to evaporate the organic solvent, resulting in appropriate electrical characteristics. Finally, the antenna prototype was created by connecting the printed antenna pattern to an SMA connector using a conductive adhesive.

The DRA was then bonded to the flexible antenna using a conductive adhesive, forming the final integrated flexible antenna prototype (Fig. 10(a)). The favorable flexibility of the antenna is shown in Fig. 10(b). Fig. 10(c) illustrates the experimental setup for measuring S_{11}. A comparison between the simulated and measured S_{11} and gain values is presented in Fig. 11. It can be observed that the measured and simulated results of the antenna in the planar state, shown in Figs. 11(a) and (b), are essentially consistent. Within the frequency range of 2.9 to 6.5 GHz, the S_{11} is less than -10 dB, and the gain reaches 3.18 dBi (3.6 GHz), 3.02 dBi (4 GHz), 4.28 dBi (4.7 GHz), and 6.12 dBi (5.8 GHz). To evaluate the flexibility of the antenna, its S_{11} performance was simulated and measured under different bending radii, as shown in Fig. 11(c). Compared with the planar state, the impedance bandwidth of the bent antenna exhibited a slight change, but it still met the design requirements.

Figure 12 shows that the measured and predicted radiation patterns at 3.6 and 4 GHz correlate well. At 4.7 and 5.8 GHz, there are differences between the measured and simulated values at $\theta = 0°$ and $\theta = 180°$ for both the E and H-plane patterns. However, in general, the detected radiation parameters met the operating requirements for omnidirectional RF-EH and specialized WPT. In Figs. 13(a)–(d), the radiation performance of the antenna remains steady for bending radii of 20 mm, 30 mm, and 40 mm.

3. RECTIFIER CIRCUIT ANALYSIS AND DESIGN

3.1. Design of Rectifier Circuit

This paper presents a broadband rectifier based on dual-channel impedance matching, which operates in the 2.5–6.6 GHz frequency band and is fabricated on a PDMS substrate. Fig. 14(a) shows a schematic of the proposed rectifier circuit. The circuit consists of a dual-channel impedance-matched rectification network, a DC-pass filter, and a load.

The key component of the rectifier is a dual-channel parallel voltage doubler (VD) architecture, in which each channel implements a fundamental VD topology. Compared with a single diode rectifier structure, the dual-channel parallel VD effectively narrows the initial impedance variation range induced

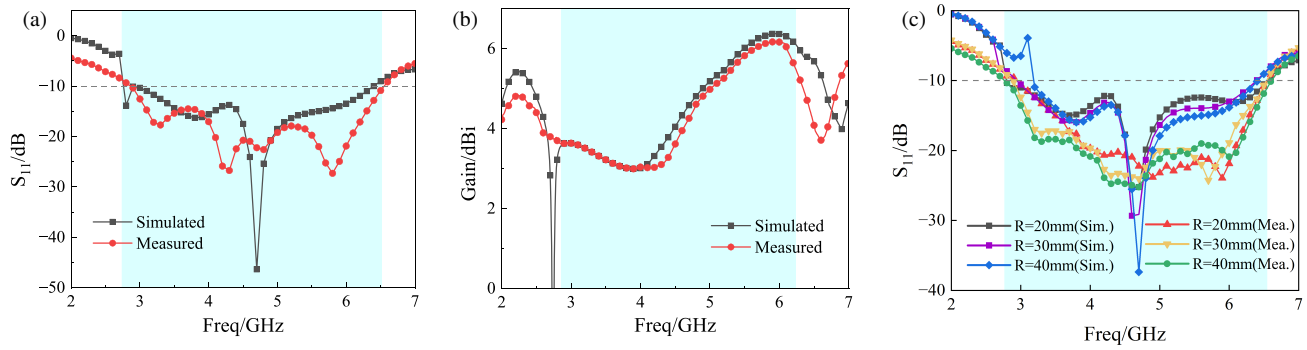

FIGURE 11. Simulated vs. measured results. (a) S_{11} in planar state. (b) Gain in the planar state. (c) S_{11} variation with bending radius ($R = 20$, 30, 40 mm).

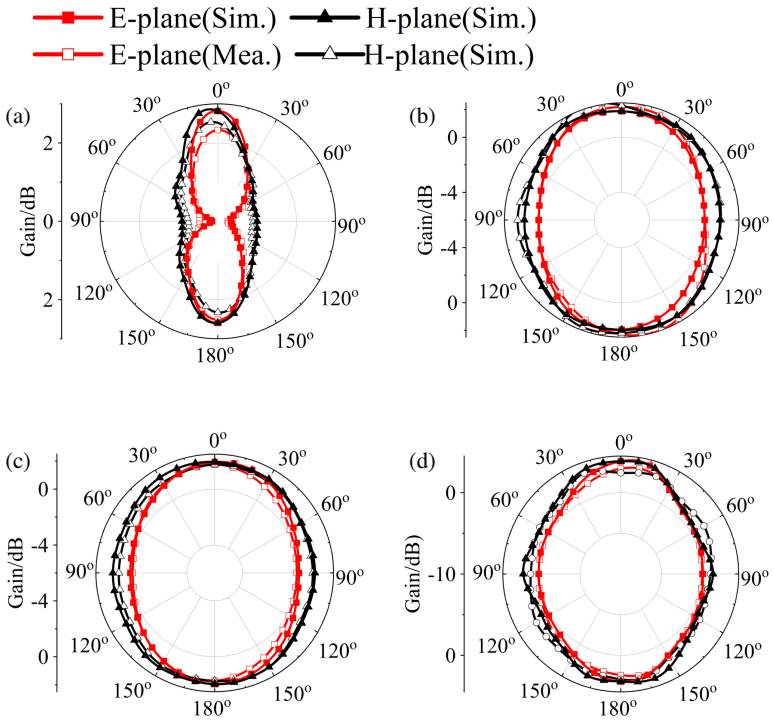

FIGURE 12. Radiation patterns are simulated and measured at (a) 4.7 GHz, (b) 3.6 GHz, (c) 4 GHz, (d) 5.8 GHz.

by the diodes and establishes a stable foundation for subsequent wideband matching.

To enhance the impedance matching in the wideband range, matching networks are introduced into dual parallel branches. By tuning microstrip lines TL1 (main branch) and TL4 (auxiliary branch), the input impedances of the two branches are compressed to approximately 50 Ω.

According to transmission line theory, the electrical length $\theta(f)$ of these lines is linearly proportional to the frequency f:

$$\theta(f) = \beta l = \frac{2\pi f\sqrt{\varepsilon_{eff}}}{c} \cdot l \tag{2}$$

where β is the phase constant; l is the physical length of the microstrip line; c and f are the speed of light in vacuum and signal frequency, respectively; and ε_{eff} denotes the effective dielectric constant of the substrate.

Equation (2) indicates that the electrical length of the microstrip line increases with frequency. Therefore, TL1 and TL4 introduce significant clockwise phase shifts at high frequencies on the Smith chart. In Fig. 15, the impedances of the initial circuit without matching networks (Rec 1) exhibit a wide dispersion between f_1 and f_2, due to the impedance deviation caused by the parasitic effects of the Schottky diode HSMS2862. By collaboratively adjusting TL1 and TL4, the impedance locus rotates clockwise, approaching 50 Ω at high frequencies while remaining stable at low frequencies, as denoted by Rec 2. Through the differential phase compensation mechanism, the initially divergent impedance variation is compressed to approximately 50 Ω, which ensures that the circuit maintains a stable impedance bandwidth and flat power conversion efficiency (PCE) across the entire operating frequency range.

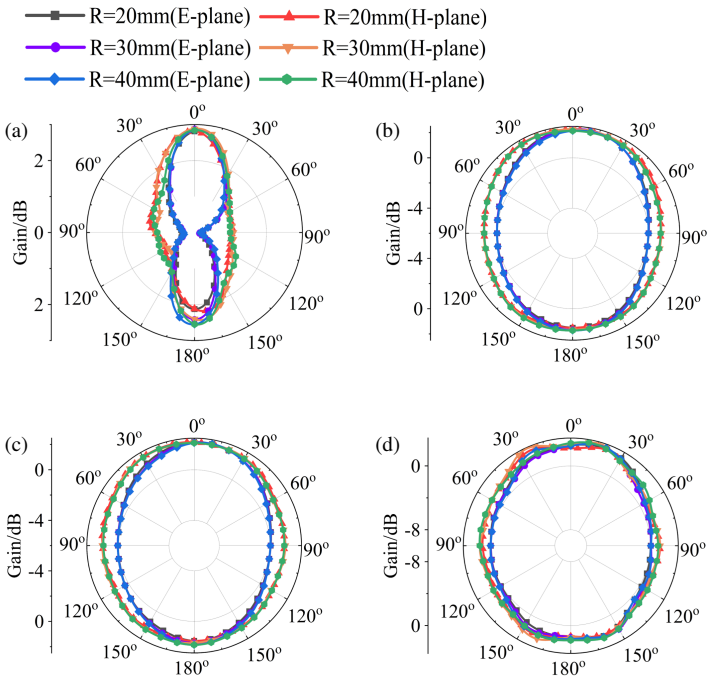

FIGURE 13. Radiation patterns at various curvature radii for different frequency bands: (a) 4.7 GHz, (b) 3.6 GHz, (c) 4 GHz, (d) 5.8 GHz.

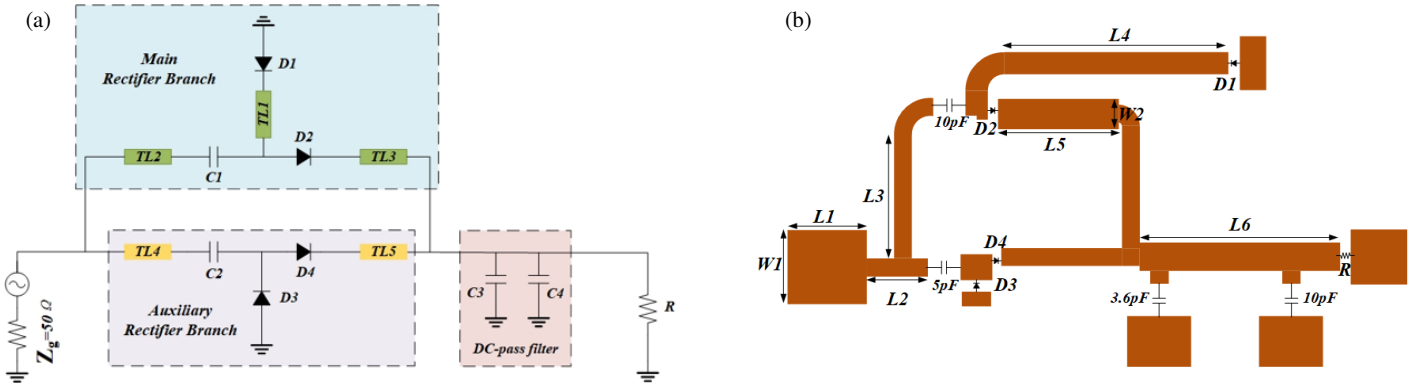

FIGURE 14. Rectifier configuration. (a) Schematic diagram. (b) Layout diagram.

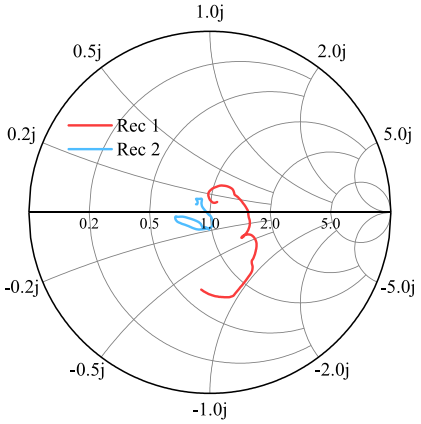

FIGURE 15. Input impedance trajectories of Rec 1 and Rec 2 from 2.5 GHz (f_1) to 6.6 GHz (f_2).

The rectifier circuit layout is depicted in Fig. 14(b), with the following optimized parameters: $W1 = 3.6$ mm, $W2 = 1.5$ mm, $L1 = 3.9$ mm, $L2 = 3.1$ mm, $L3 = 6$ mm, $L4 = 11$ mm, $L5 = 6$ mm, $L6 = 10$ mm. Fig. 16(a) shows the S-parameters as functions of the input power and frequency. Figs. 16(b) and (c) show that the efficiency increases with the input power across the three design bands, attaining peaks at 3.6 GHz (18 dBm), 4.7 GHz (19 dBm), and 5.8 GHz (15 dBm). As the input power continues to increase, the efficiency begins to decline owing to the device's nonlinearity effects. The rectifier achieved peak efficiencies of 61.7%, 65.7%, and 58.4% at 3.6, 4.7, and 5.8 GHz, respectively.

3.2. Test of Rectifier Circuit

The rectifier circuit was fabricated, and the resulting physical assembly is shown in Fig. 17. Owing to the difficulty of adhering liquid metal to PDMS through holes, silver wires were used to pass through the flexible PDMS substrate to form vias. Two silver wires were used at the load end of the rectifier circuit to facilitate rectified voltage measurement. This design

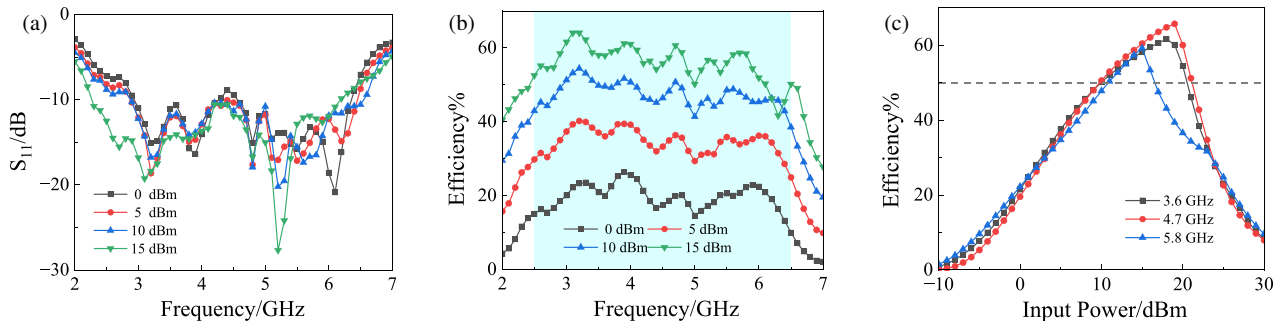

FIGURE 16. Simulated rectifier performance. (a) S_{11} of the rectifier circuit. (b) Efficiency vs freq. (c) Efficiency vs input power.

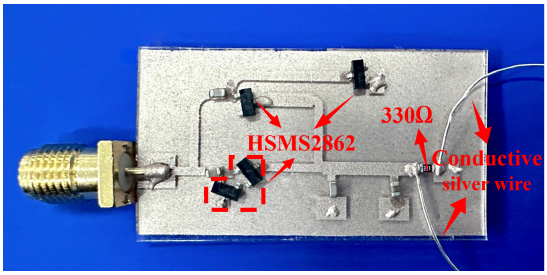

FIGURE 17. The photograph of the rectifier circuit.

also highlights the feasibility of integrating liquid metal-based components with flexible substrates, offering both mechanical flexibility and electrical efficiency.

After fabricating the flexible rectifier circuit, its performance was experimentally characterized. The simulated and measured PCE at 3.6, 4.7, and 5.8 GHz is shown in Fig. 18. Peak efficiencies of 52.1% (3.6 GHz), 57.9% (4.7 GHz), and 46.9% (5.8 GHz) were have been observed. The discrepancy between the measured and simulated results is mainly attributed to the parasitic inductance of silver wire vias, fabrication tolerances, and the parasitic effects associated with the diode and capacitor components.

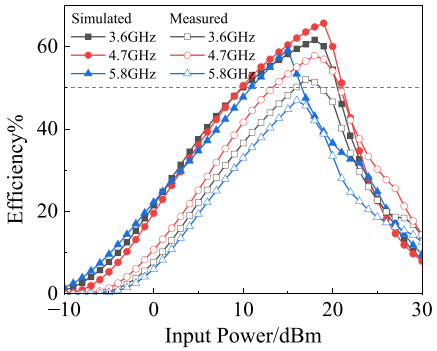

FIGURE 18. Simulated and measured PCEs.

4. RECTENNA TESTING AND ANALYSIS

The antenna and rectifier were co-fabricated on the same flexible substrate, with overall dimensions of 60 mm × 25 mm. The experimental setup is illustrated in Fig. 19.

A test setup was built to evaluate the overall performance of the rectenna system, as shown in Fig. 20. An RF signal at the desired frequency was generated using a signal generator and amplified using a power amplifier. The transmitting antenna then radiated the signal to the far field, where it was picked up by the receiving antenna and fed into the rectifier circuit to be converted into a DC signal, which was then delivered to the load. The far-field region is defined as the area where the distance from the transmitting antenna is greater than $2D_{\max}^2/\lambda$, where $D_{\max}$ denotes the maximum geometric dimension of the transmitting and receiving antennas, and λ represents the free-space wavelength corresponding to the operating frequency. Accordingly, the distance between the rectenna and transmitting antenna was set to 164 cm.

The PCE of the rectenna is defined as in (3):

$$\eta = \frac{P_{out}}{P_{in}} \times 100\% = \frac{V_{out}^2}{R \cdot P_{in}} \times 100\% \tag{3}$$

where P_{out} is the DC power output of the rectenna, P_{in} the received power of the rectenna, R the load at the output of the rectifier circuit, and V_{out} the voltage across the load [29]. The PCE of the rectenna measured at various input powers over a broad frequency range is shown in Fig. 21(a). The rectenna achieved a conversion efficiency of more than 45% when the input power was 15 dBm. In Fig. 21(b), the PCE of the rectenna decreases under different bending radii by no more than 5% compared with the flat state, demonstrating its stable performance under bending conditions. This enables the rectenna to be integrated onto non-planar surfaces, such as robotic arms and curved sensor housings, without sacrificing RF-EH and WPT performance.

The performance of the proposed hybrid rectenna is compared with that of other related works in Table 2. The rectennas in [8, 11, 28] feature omnidirectional or directional beams, along with compact size or flexibility, but none possess directional WPT capability. Moreover, their RF-EH bandwidths are narrow. Some studies have realized both RF-EH and WPT, but the rigid structure in [20] and the large design in [21] limit their practical applications. Compared with [20], the proposed hybrid antenna achieves a higher gain and wider bandwidth, with a corresponding rectifier integrated to realize a hybrid rectenna system. [20] only presents a hybrid antenna without a corresponding rectifier. In summary, the proposed design achieves a favorable balance among wideband RF-EH, directional WPT, flexibility, and compactness, while enabling conformal attachment to curved surfaces.

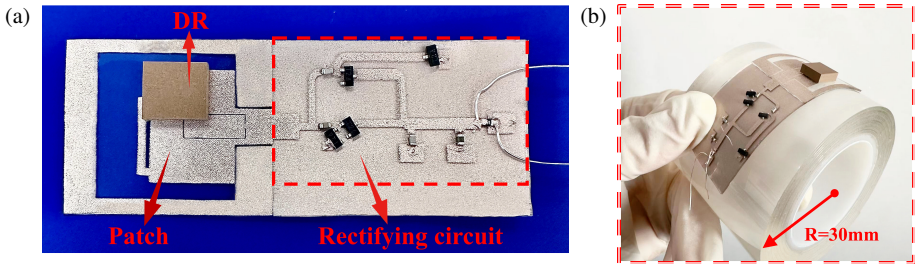

FIGURE 19. The photograph of the rectenna. (a) Rectenna on a plane surface. (b) Rectenna on a curved surface.

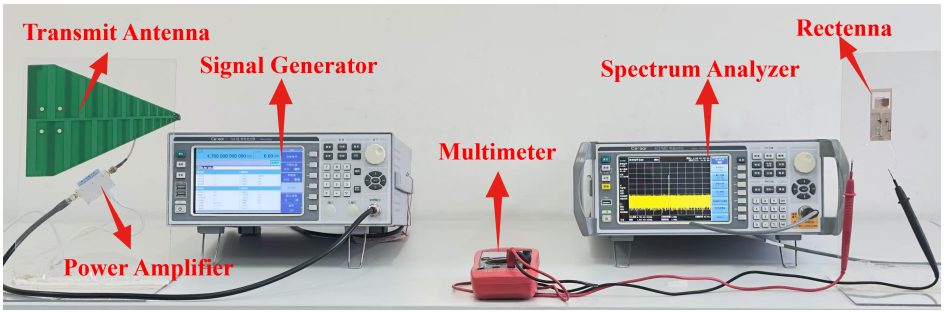

FIGURE 20. Rectenna testing system.

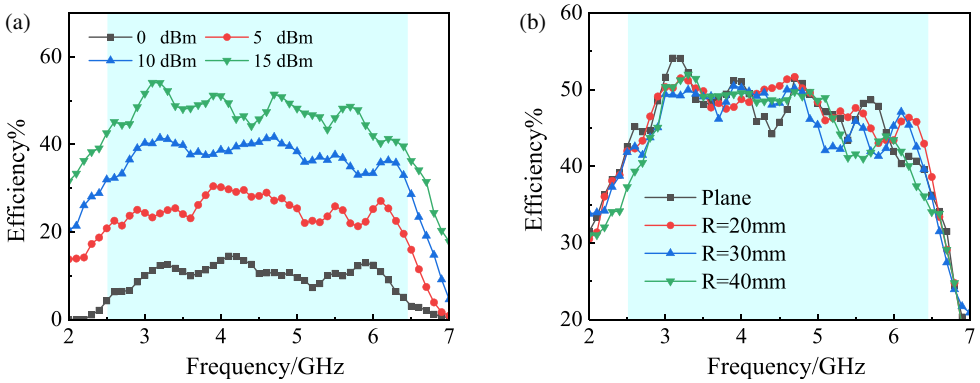

FIGURE 21. The PEC measurement results of rectenna. (a) The PCE at different input powers. (b) The PCE at different radii of curvature.

TABLE 2. Performance comparison with previous works.

Ref.	Freq. (GHz)	Flexibility	Gain (dBi)	Beams	Peak PCE @Input Power	Antenna Size (mm × mm)
[8]	0.9/1.8/2.45/5.8	Yes	−2.7/3.4/4.2/4.8	bidirectional	50% @5 dBm	105 × 82
[11]	2.07–2.57	No	2.07–4.55	omnidirectional	72.47% @10 dBm	50 × 44
[20]	2.03–4.08/5.8	No	−0.42–0.91 for RF-EH/2.4 for WPT	omni/bi-directional	without rectifier	42.6 × 32.6
[21]	1.55–3.61/5.8	No	1.56–4.17 for RF-EH/12.73 for WPT	omni/bi-directional	65% @11 dBm	$55^2\pi$
[28]	2.4	Yes	5.7	directional	49.4% @13 dBm	240 × 240
This work	**2.8–6.3/4.7**	**Yes**	**2.82–6.36 for RF-EH/4.28 for WPT**	**omni/directional**	**57.9% @15 dBm**	**30 × 25**

5. CONCLUSION

This study proposes a flexible hybrid rectenna that integrates omnidirectional RF-EH with directional WPT using a frequency-domain complementary scheme. The CPW-fed notched broadband microstrip antenna provides an omnidirectional coverage from 2.8 to 6.3 GHz with a notch at 4.7 GHz. At 4.7 GHz, the split-ring slot region and the gap between the L-shaped strip and the radiation element jointly act as a feed to excite the DRA's TM^{z}_{201} mode. In this mode, the DRA can be equivalently modeled as a magnetic dipole array, generating a directional beam of 4.28 dBi. The suggested hybrid rectenna attained a high PCE of 57.9% combined with a broadband rectifier. By integrating the system on a PDMS substrate, an excellent trade-off was achieved among broadband RF-EH, directional WPT, flexible conformability, and structural compactness, demonstrating strong potential for conformal IoT devices, curved communication nodes, and miniaturized sensors.

ACKNOWLEDGEMENT

This work was supported by the Liaoning Provincial Department of Education Basic Research Funding Program under Grant (LJ232410147074).

REFERENCES

[1] Zhou, I., I. Makhdoom, N. Shariati, M. A. Raza, R. Keshavarz, J. Lipman, M. Abolhasan, and A. Jamalipour, "Internet of things 2.0: Concepts, applications, and future directions," *IEEE Access*, Vol. 9, 70 961–71 012, 2021.

[2] Ullah, M. A., R. Keshavarz, M. Abolhasan, J. Lipman, K. P. Esselle, and N. Shariati, "A review on antenna technologies for ambient RF energy harvesting and wireless power transfer: Designs, challenges and applications," *IEEE Access*, Vol. 10, 17 231–17 267, 2022.

[3] Kim, S.-J., S. Kim, J.-H. Lee, and J.-W. Yu, "A compact broadband stepped bow-tie antenna for ambient RF energy harvesting," *IEEE Access*, Vol. 11, 60 365–60 373, 2023.

[4] Das, R., M. V. Swati, and G. S. Baghel, "Highly efficient, broadband, hexagonal shaped rectenna for energy harvesting in IoT applications," *AEU — International Journal of Electronics and Communications*, Vol. 201, 155957, 2025.

[5] Shi, Y., J. Jing, Y. Fan, L. Yang, Y. Li, and M. Wang, "A novel compact broadband rectenna for ambient RF energy harvesting," *AEU — International Journal of Electronics and Communications*, Vol. 95, 264–270, 2018.

[6] Shi, Y., Y. Fan, Y. Li, L. Yang, and M. Wang, "An efficient broadband slotted rectenna for wireless power transfer at LTE band," *IEEE Transactions on Antennas and Propagation*, Vol. 67, No. 2, 814–822, 2019.

[7] Muhammad, S., J. J. Tiang, S. K. Wong, A. Smida, R. Ghayoula, and A. Iqbal, "A dual-band ambient energy harvesting rectenna design for wireless power communications," *IEEE Access*, Vol. 9, 99 944–99 953, 2021.

[8] Wang, C., J. Zhang, S. Bai, D. Chang, and L. Duan, "A multiband compact flexible energy collector for wearable or portable IoT devices," *IEEE Antennas and Wireless Propagation Letters*, Vol. 22, No. 5, 1164–1168, 2023.

[9] Yang, Y., J. Li, L. Li, Y. Liu, B. Zhang, H. Zhu, and K. Huang, "A 5.8 GHz circularly polarized rectenna with harmonic suppression and rectenna array for wireless power transfer," *IEEE Antennas and Wireless Propagation Letters*, Vol. 17, No. 7, 1276–1280, 2018.

[10] Sang, J., L. Qian, X. Wang, M. Li, J. Wang, G. Shi, and Z. Zhu, "A triple-band and high-gain circularly polarized rectenna for radio-frequency energy harvesting applications," *IEEE Transactions on Antennas and Propagation*, Vol. 73, No. 8, 5223–5238, 2025.

[11] Zhou, Z., W. Lin, and Y.-X. Sun, "Wideband circularly polarized high-efficiency rectenna with large-angle wireless power capture capability," *IEEE Antennas and Wireless Propagation Letters*, Vol. 23, No. 12, 4428–4432, 2024.

[12] Zhang, W., J. Zhang, C. Song, R. Pei, X. Zhang, H. Liu, C. Han, Y. Huang, and J. Zhou, "Aperture sharing metasurface-based wide-beam antenna for energy harvesting," *AEU — International Journal of Electronics and Communications*, Vol. 173, 155009, 2024.

[13] Wagih, M., A. S. Weddell, and S. Beeby, "Omnidirectional dual-polarized low-profile textile rectenna with over 50% efficiency for sub-μw/cm^2 wearable power harvesting," *IEEE Transactions on Antennas and Propagation*, Vol. 69, No. 5, 2522–2536, 2021.

[14] Pathak, S., J. Singh, A. Patnaik, A. K. Gautam, and T. Goel, "Wideband hybrid AEH system: Exploring transparent and opaque materials for sustainable power solutions in small gadgets," *AEU — International Journal of Electronics and Communications*, Vol. 201, 155973, 2025.

[15] Wagih, M., G. S. Hilton, A. S. Weddell, and S. Beeby, "Millimeter-wave power transmission for compact and large-area wearable IoT devices based on a higher order mode wearable antenna," *IEEE Internet of Things Journal*, Vol. 9, No. 7, 5229–5239, 2022.

[16] Qi, X., Z. Xu, and H. Li, "High-efficiency 2-D multibeam rectenna based on gain enhanced patch array," *IEEE Antennas and Wireless Propagation Letters*, Vol. 21, No. 12, 2537–2541, 2022.

[17] Boussaadia, Y., M. Tellache, and F. Amrani, "A novel high-gain rectenna for wireless power transmission (WPT) applications," *International Journal of Communication Systems*, Vol. 38, No. 9, e70112, 2025.

[18] Lu, X., P. Wang, D. Niyato, D. I. Kim, and Z. Han, "Wireless networks with RF energy harvesting: A contemporary survey," *IEEE Communications Surveys & Tutorials*, Vol. 17, No. 2, 757–789, 2015.

[19] Li, H. and W. Lin, "An electrically small, pattern-reconfigurable, HCP antenna with quasi-isotropic beam coverage for wireless power transfer enabled IoT applications," *IEEE Internet of Things Journal*, Vol. 13, No. 6, 12 169–12 177, 2026.

[20] Zhang, P., H. Yi, H. Liu, H. Yang, G. Zhou, and L. Li, "Back-to-back microstrip antenna design for broadband wide-angle RF energy harvesting and dedicated wireless power transfer," *IEEE Access*, Vol. 8, 126 868–126 875, 2020.

[21] Lu, Z. F., J. Liu, and B. X. Liu, "A hybrid high-efficiency rectenna for simultaneously dedicated single-band WPT and broadband omnidirectional RF energy harvesting," *IEEE Transactions on Antennas and Propagation*, Vol. 74, No. 2, 2113–2118, 2026.

[22] Liu, S.-B., F.-S. Zhang, M. Boyuan, S.-P. Gao, and Y.-X. Guo, "Multiband dual-polarized hybrid antenna with complementary beam for simultaneous RF energy harvesting and WPT," *IEEE Transactions on Antennas and Propagation*, Vol. 70, No. 9, 8485–8495, 2022.

[23] Sharma, P. K., N. Gupta, and P. I. Dankov, "Analysis of dielectric properties of polydimethylsiloxane (PDMS) as a flexible

substrate for sensors and antenna applications," *IEEE Sensors Journal*, Vol. 21, No. 17, 19 492–19 504, 2021.

[24] Zhuang, Z., X. Xuan, H. Li, D. Jiang, and M. Li, "A wearable antenna sensor based on ePDA/SiO_2 nanowalls for the detection of lactic acid in sweat," *Sensors and Actuators B: Chemical*, Vol. 404, 135265, 2024.

[25] Wang, Z., D. Lu, R. Li, and Y. Yu, "Flexible broadband rectifying array antenna based on printed liquid metal," *IEEE Transactions on Microwave Theory and Techniques*, Vol. 73, No. 9, 6001–6008, 2025.

[26] Yu, B.-Y., Z.-H. Wang, L. Ju, C. Zhang, Z.-G. Liu, L. Tao, and W.-B. Lu, "Flexible and wearable hybrid RF and solar energy harvesting system," *IEEE Transactions on Antennas and Propagation*, Vol. 70, No. 3, 2223–2233, 2022.

[27] Wang, T.-S., C.-Z. Du, H.-F. Shu, and Z.-H. Yue, "A flexible UWB slot antenna with quad band-notched characteristics for wearable application," *Progress In Electromagnetics Research C*, Vol. 140, 127–134, 2024.

[28] Zada, M., U. R. Iman, A. Basir, and H. Yoo, "Battery-free digitally embroidered smart textile energy harvester for wearable healthcare IoTs," *IEEE Transactions on Industrial Electronics*, Vol. 71, No. 8, 9865–9874, 2024.

[29] Li, L., X. Li, L. Wang, Y. Jia, Y. Hu, and J. Nan, "High gain nested dielectric resonator rectenna based on higher order mode and magneto-electric dipole theory," *AEU — International Journal of Electronics and Communications*, Vol. 188, 155590, 2025.